Journal of Energy Chemistry 56 (2021) 72–79

Contents lists available at ScienceDirect

Journal of Energy Chemistry

journal homepage: www.elsevier.com/locate/jechem

http://www.journals.elsevier.com/journal-of-energy-chemistry/

Ultrafine Fe/Fe_3C decorated on Fe-N_x-C as bifunctional oxygen electrocatalysts for efficient Zn-air batteries

Lingbo Zong [a], Xin Chen [a], Siliang Liu [b], Kaicai Fan [c,*], Shuming Dou [b], Jie Xu [b], Xiaoxian Zhao [d], Wenjun Zhang [e], Yaowen Zhang [a], Weicui Wu [a], Fenghong Lu [a], Lixiu Cui [a], Xiaofei Jia [a], Qi Zhang [a], Yu Yang [a], Jian Zhao [e], Xia Li [f], Yida Deng [b], Yanan Chen [b,*], Lei Wang [a,*]

[a] *Taishan Scholar Advantage and Characteristic Discipline Team of Eco Chemical Process and Technology, Key Laboratory of Optic-electric Sensing and Analytical Chemistry for Life Science, MOE, State Key Laboratory of Eco-chemical Engineering, College of Chemistry and Molecular Engineering, Qingdao University of Science and Technology, Qingdao 266042, Shandong, China*

[b] *School of Materials Science and Engineering, Key Laboratory of Advanced Ceramics and Machining Technology of Ministry of Education, Tianjin Key Laboratory of Composite and Functional Materials, Tianjin University, Tianjin 300072, China*

[c] *Centre for Clean Environment and Energy, School of Environment and Science, Griffith University, Queensland 4222, Australia*

[d] *College of Science, Hebei Agricultural University, Baoding 071001, Hebei, China*

[e] *Key Laboratory of Rubber-Plastics, Ministry of Education/Shandong Provincial Key Laboratory of Rubber-Plastics, Qingdao University of Science and Technology, Qingdao 266042, Shandong, China*

[f] *College of Materials Science and Engineering, Qingdao University of Science & Technology, Qingdao 266042, Shandong, China*

ARTICLE INFO

Article history:
Received 25 February 2020
Revised 21 July 2020
Accepted 22 July 2020
Available online 31 July 2020

Keywords:
Non-precious metal
Nitrogen-rich carbon
Fe/Fe_3C
Fe-N_x-C
Bifunctional oxygen electrocatalysts

ABSTRACT

Efficient bifunctional oxygen electrocatalysts for ORR and OER are fundamental to the development of high performance metal-air batteries. Herein, a facile cost-efficient two-step pyrolysis strategy for the fabrication of a bifunctional oxygen electrocatalyst has been proposed. The efficient non-precious-metal-based electrocatalyst, Fe/Fe_3C@Fe-N_x-C consists of highly curved onion-like carbon shells that encapsulate Fe/Fe_3C nanoparticles, distributed on an extensively porous graphitic carbon aerogel. The obtained Fe/Fe_3C@Fe-N_x-C aerogel exhibited superb electrochemical activity, excellent durability, and high methanol tolerance. The experimental results indicated that the assembly of onion-like carbon shells with encapsulated Fe/Fe_3C yielded highly curved carbon surfaces with abundant Fe-N_x active sites, a porous structure, and enhanced electrocatalytic activity towards ORR and OER, hence displaying promising potential for application as an air cathode in rechargeable Zn-air batteries. The constructed Zn-air battery possessed an exceptional peak power density of ~147 mW cm^{-2}, outstanding cycling stability (200 cycles, 1 h per cycle), and a small voltage gap of 0.87 V. This study offers valuable insights regarding the construction of low-cost and highly active bifunctional oxygen electrocatalysts for efficient air batteries.

1. Introduction

The emerging energy crisis and escalating environmental degradation, resulting from the burning of fossil fuels, has accelerated the exploration of renewable energy conversion and storage technologies. Rechargeable Zn-air batteries, possessing a high theoretical specific energy density, represent a promising alternative for next-generation energy conversion devices [1–3]. However, power density and efficiency of Zn-air batteries are drastically impeded by sluggish oxygen reduction reaction (ORR) and oxygen evolution reaction (OER) rates, occurring at the air electrode [4]. Therefore, the development of electrocatalysts capable of efficient ORR and OER is crucial for the realization of practical applications of Zn-air batteries. Currently, precious-metal-based high-performing oxygen electrocatalysts are considered as state-of-the-art [5]. Nevertheless, their large-scale application is substantially restricted by their prohibitive cost [6]. Hence, the development of low-cost non-precious-metal-based electrocatalysts, with excellent catalytic properties toward ORR and OER, is critical for realizing commercial applications of Zn-air batteries.

In recent years, 3*d* transition metals (TMs) and their alloys have been investigated as efficient ORR and OER electrocatalysts [7–11].

* Corresponding authors.
E-mail addresses: kaicai.fan@griffithuni.edu.au (K. Fan), yananchen@tju.edu.cn (Y. Chen), inorchemwl@126.com (L. Wang).

https://doi.org/10.1016/j.jechem.2020.07.048
2095-4956/

However, these TM nanoparticles possess low concentrations of catalytically active sites, are prone to aggregate, and do not offer a competitive advantage for electrocatalytic applications. In addition to alleviating crystallite dissolution and agglomeration during electrochemical reactions, hybrid carbon materials have recently been shown to increase the exposure of catalytically active sites, as well as facilitate electrocatalytic reaction pathways [12–14]. Although the catalytic site characteristics of the composites remain debatable, both metallic clusters and M-N_x-C moieties have been shown to contribute to the enhancement of electrochemical performance [15,16]. While it is challenging to preserve nature of active sites (e.g. metallic nanoparticles) by simply incorporating with carbon materials, since the naked metal nanoparticles are not stable enough during ORR, and will experience oxygen-induced degradation and deterioration of electrochemical activity [17]. Close proximity between the metallic nanoparticle core and onion-like carbon shell, bearing abundant M-N_x-C sites, promotes synergistic catalysis and contributes to the enhancement of catalytic performance. Such an arrangement facilitates electron transfer from the metal nanoparticle core to the carbon shell, allowing the electronic properties of the carbon shell to be modified, which consequently alters the binding energies of reaction intermediates and enhances electrochemical performance [17,18]. Furthermore, the highly curved carbon support anchoring individual metal sites enables the combination of efficient charge transfer and a strong electric field effect for electrocatalysis, which further promotes reaction kinetics [19]. Hence, the encapsulation of metal cores by highly curved carbon shells bearing atomically dispersed metal sites, endows the catalyst with dense and efficient active sites for enhanced electrochemical performance. Though advances on carbon incorporated metal nanoparticles have been made recently, facile and efficient strategy to achieve highly curved carbon shells encased metallic nanoparticles with excellent electrochemical activity towards ORR is still challenging.

Herein, a facile two-step pyrolysis strategy for the fabrication of the bifunctional oxygen electrocatalyst, Fe/Fe_3C@Fe-N_x-C, is disclosed, wherein uniform Fe/Fe_3C nanocrystals were encapsulated by onion-like carbon shells and distributed on a highly porous carbon aerogel. The controlled carbonization procedure affords the formation of specific structure in which defined Fe/Fe_3C nanoparticles were tightly encased by carbon shells. Such close proximity between the highly curved carbon shells possessing abundant Fe-N_x-C moieties and the Fe/Fe_3C nanoparticles promotes synergistic catalysis and contributes to enhanced catalytic performance for both ORR and OER. Benefiting from its three dimensional (3D) porous structure, abundant exposed active sites, and modified electronic structure, the as-synthesized Fe/Fe_3C@Fe-N_x-C displayed excellent ORR performance with 4 electron reaction selectivity, favorable activity, outstanding robustness and excellent methanol tolerance. Moreover, the catalyst exhibited an onset potential of 1.0 V, a half-wave potential of 0.9 V for ORR, and a low potential of 1.64 V at 10 mA cm^{-2} for OER. The utilization of the fabricated catalyst as an air cathode in a constructed rechargeable Zn-air battery, delivered a high peak power density of ~147 mW cm^{-2} and remarkable stability over 200 cycles (1 h per cycle) at a current density of 5 mA cm^{-2}. Overall, a novel, facile cost-effective strategy is presented for the development of exceptionally efficient bifunctional oxygen electrocatalysts for improved Zn-air batteries.

2. Material and methods

2.1. Materials

Analytical grade $NaNO_3$, $FeCl_3{\cdot}6H_2O$, KOH, EDTA-4Na, and HCl were purchased from the Sinopharm Chemical Reagent Co., Ltd. Commercial Pt/C, Nafion solution, and RuO_2 were acquired from Sigma-Aldrich and/ or Alfa Aesar. All chemicals were used as received.

2.2. Synthesis of the catalyst

2.2.1. Synthesis of EDTA-Fe

In a typical procedure, $FeCl_3{\cdot}6H_2O$ (0.550 g) was dissolved in 2.5 mL of deionized water (DI water); then EDTA-4Na (1.9 g) in 5 mL of NaOH (1 mol L^{-1}) was injected into the $FeCl_3$ solution under vigorous stirring at 100 °C, until a yellow power formed. The obtained complex was denoted as EDTA-Fe.

2.2.2. Synthesis of the Fe/Fe_3C@Fe-N_x-C aerogel

Typically, EDTA-Fe (50 mg), glucose (360 mg), and $NaNO_3$ (420 mg) were dispersed in 6 mL of DI water. Next, 3 mL of HCl (1 mol L^{-1}) containing melamine (504 mg) was added to the above solution and the resulting mixture was stirred at room temperature. The vial containing the hydrogel was then subjected to lyophilization. The dried gel was placed into a tube furnace and heated to 280 °C for 6 h at a heating rate of 5 °C min^{-1} under a flow of N_2. The obtained product was washed with DI water several times to remove remaining salts, and the products were dried under vacuum for 10 h before the second pyrolysis step. The dried product was heated in a tube furnace under N_2 at 950 °C (5 °C min^{-1}) for 2 h and allowed to cool to room temperature to obtain the final aerogel.

2.2.3. Synthesis of N-doped carbon electrocatalyst N-C

The N-doped carbon electrocatalyst (N-C) was fabricated according to the protocol for Fe/Fe_3C@Fe-N_x-C synthesis, without the introduction of EDTA-Fe.

2.3. Characterization

Powder X-ray diffraction patterns of the as-prepared electrocatalysts were performed on a Rigaku-Dmax 2500 diffractometer with Cu-$K\alpha$ radiation. The morphologies and structural information of the synthesized electrocatalysts were analyzed via scanning electron microscopy (SEM, FE-SEM, S4800, Hitachi) and transmission electron microscopy (TEM, JEM-2100F). X-ray photoelectron spectroscopy (XPS, Kratos Axis ULTRA) was implemented to evaluate the chemical compositions of the obtained catalysts. Pore distribution and specific surface area were determined from nitrogen adsorption–desorption curves at 77 K, employing the ASAP 2020 physisorption analyzer (Micrometrics). Raman spectroscopy was performed on a confocal Raman microscope (LabRAM HR800).

2.4. Electrochemical characterization

Electrochemical characteristics were investigated on an electrochemical workstation (CHI 760E, Princeton: PARSTAT MC), consisting of a rotating disk electrode (RDE) and a rotating ring-disk electrode (RRDE) (Pine Instrument Company, USA). For ORR, Pt wire, a glassy carbon electrode with a diameter of 5 mm (5.61 mm for the glassy carbon electrode including the Pt ring), and a Ag/AgCl (with saturated KCl solution) electrode were used as the counter, working, and reference electrodes, respectively. For the OER, Pt wire, a glassy carbon electrode, and a Hg/HgO electrode were used as the counter, working, and reference electrodes, respectively. Typically, the electrocatalyst ink was prepared by adding electrocatalyst (5.0 mg) to a mixture of Nafion solution (40 μL), deionized water (720 μL), and isopropyl alcohol (240 μL), followed by ultrasonication for 30 min. Then, the freshly-prepared electrocatalyst ink was deposited onto the glassy carbon electrode with a controlled loading of 0.51 mg cm^{-2} and dried at room temperature. The loading capacity of benchmark

noble metals is similarly 0.51 mg cm^{-2}. Prior to measurement, the glassy carbon working electrode was cycled several times until a repeatable capacitance was attained. The ORR polarization curves were obtained from 1.2 to 0.2 V (vs. RHE) with a scan rate of 5 mV s^{-1}. The potentials were calculated using the equation: E (RHE) = E(Ag/AgCl) + 0.059 pH + 0.1976 – 95% iR. Four-electron selectivity and H_2O_2 yield during the ORR were determined by measured ring and disk currents. The OER polarization curves with 95% iR-compensation were determined from 1.2 to 1.8 V (vs. RHE) in 1.0 M KOH solution with a scan rate of 5 mV s^{-1}, and a rotation rate of 1600 rpm. Potentials were calculated using the equation: E_{RHE} (V) = $E_{Hg/HgO}$ + 0.926

2.5. Zn-air battery

To fabricate the aqueous Zn-air battery, the catalyst ink was first prepared by sonicating 10 mg of catalyst and 30.0 μL of 5 wt% Nafion solution in 970.0 μL of isopropanol for 1 h. The as-prepared catalyst ink solution was sprayed onto carbon paper, followed by drying at 60 °C for 2 h, and then used as the air cathode. The loading amount for all catalysts was 1 mg cm^{-2}. A Zn plate was applied as the anode. Zn-air battery tests were performed on self-manufactured cells using the two electrodes and 6.0 M KOH electrolyte solution at room temperature.

3. Results and discussion

Fig. 1(a) briefly describes the synthetic approach for the production of Fe/Fe_3C@Fe-N_x-C. The electrocatalyst, bearing copious active sites and Fe/Fe_3C nanocrystals encapsulated by nitrogen-rich carbon shells, was derived via pyrolysis of the sol–gel precursor. First, a given amount of EDTA-4Na-coordinated $FeCl_3$ was added to the melamine solution and the resultant mixture was stirred at room temperature to obtain a light-yellow hydrogel. Then, the lyophilized hydrogel (Fig. S1) was subjected to two-step pyrolysis under N_2 atmosphere, to afford the Fe/Fe_3C@Fe-N_x-C aerogel. During pyrolysis, the EDTA-Fe complex is carbonized in-situ to generate onion-like carbon shells that encapsulate the Fe/Fe_3C nanocrystals, and coupled with Fe, the N co-doped carbon aerogel.

The Fe/Fe_3C@Fe-N_x-C aerogel obtained at 950 °C was first characterized by SEM, and the results are shown in Fig. 1(b). SEM images revealed a 3D porous structure and the absence of distinguishable carbon nanotubes. It has been demonstrated that transition-metal salts, especially those of Fe, catalyze the carbon nanotubes during pyrolysis [20]. Accordingly, the two-step pyrolysis strategy facilitated the construction of onion-like carbon shells encapsulating Fe/Fe_3C nanoparticles, and inhibited the growth of carbon tubes.

TEM images (Fig. 1(c)) further confirmed that the porous sheet-like structure was composed of ultrathin and wrinkled carbon nanosheets. As mentioned, the melamine-based composites decompose during the pyrolysis process, producing a large amount of NH_3. Thus, in addition to melamine serving as the nitrogen source, it contributes to the formation of ultrathin crumpled carbon nanosheets. SEM and TEM images of the hydrogel and electrocatalysts prepared at various temperatures were obtained to investigate the formation of a highly porous architecture. SEM images of the obtained aerogel (Fig. S1) indicated that it was constructed from well-defined nanorods, which had a diameter of ~100 nm. Notably, the nanorods were largely bonded together to form nanosheet-like structures, contributing to the generation of carbon nanosheets following pyrolysis. As shown in Figs. S2 and S3(a), the Fe/Fe_3C nanocrystals are embedded in the carbon aerogel during pyrolysis, while thin carbon nanosheets and a porous structure are evident at higher pyrolysis temperatures. Therefore, the highly porous carbon aerogel constructed by ultrathin carbon nanosheets obtained at higher pyrolysis temperatures is expected to provide abundant exposed active sites towards ORR/OER, and enhance ion and electron transport during electrocatalytic reactions.

High-resolution TEM further elucidated the morphology and crystal structure of the embedded nanocrystals. As depicted in Fig. 1(d) and Fig. S3(b), the crystallized nanocrystals were well-encapsulated by several layers of onion-like carbon shells; the nanocrystal lattice distance was determined to be 0.20 nm, corresponding to the d-spacing of the (110) crystallographic plane of Fe, or the (220) plane of Fe_3C. High-angle annular dark-field scanning transmission electron microscopy (HAADF-STEM) results, illustrated in Fig. 1(e), confirm the presence of copious Fe/Fe_3C nanoparticles. The formation of a hierarchical morphology consisting of carbon shell-wrapped nanoparticles is presumably initiated during first low-temperature pyrolysis, when glucose and the EDTA-Fe complex are thermally decomposed and carbonized. Therefore, carbon nanotube growth was expected to cease, as the carbon layers completely enveloped the initially exposed metal nanoparticles. Subsequently, the crystallization of Fe/Fe_3C and formation of well-graphitized carbon shells occurred simultaneously, without nucleation of carbon nanotubes during the second pyrolysis. The highly curved carbon shells that anchor single metal sites enable the combination of efficient charge transfer and a strong electric field effect within the electrocatalyst, thereby promoting favorable reaction kinetics [21]. Meanwhile, Fe/Fe_3C nanoparticles are proposed to modify the electronic properties of the carbon shells, thereby altering the binding energies of reaction intermediates to facilitate the electrochemical reaction.

Energy-dispersive spectroscopy elemental mapping (Fig. 1(f, g, h)) was conducted to reveal element distribution, and to investigate possible active species of the composites. The results indicated a uniform distribution of N and C throughout the nanosheets. Fe was dispersed throughout the architecture, though it was predominantly distributed over the nanoparticles, suggesting that in addition to its nanoparticle form, Fe was present in the form of iron and nitrogen-doped carbon (Fe-N_x-C). Accordingly, the 3D nanosheets served as an outstanding carbon matrix for hosting dispersed Fe-N_x-C and Fe/Fe_3C nanoparticles, thereby maximizing active site density and promoting electrocatalytic efficiency.

To further elucidate the composition and phase structure of the electrocatalyst, X-ray diffraction (XRD) were measured and presented in Fig. 2(a). The XRD pattern displayed evident graphitic carbon peaks, and signals corresponding to cubic Fe (PDF No. 06-0696), and Fe_3C (PDF No. 35-0772). It has been established that Fe_3C nanoparticles originate from the reduction of Fe by carbon during heat treatment [21]. Raman spectroscopy was performed to investigate the Fe/Fe_3C@Fe-N_x-C carbon structure. As seen in Fig. 2(b), the Raman spectrum exhibited characteristic D (1350 cm^{-1}), and G (1600 cm^{-1}) bands, indicating disordered carbon structures with abundant defects [22]. To further evaluate the role of the N species, X-ray photoelectron spectroscopy (XPS) was conducted, and the results are demonstrated in Fig. 2(c). The high-resolution N 1*s* XPS spectrum exhibited four representative peaks, arising from graphitic-N (401.2 eV), pyrrolic-N (399.6 eV), Fe-N_x (398.8 eV), and pyridinic-N (398.1 eV) [23]. Reportedly, increased pyridinic-N and Fe-N_x site density enhances ORR and OER activities [24]; while high-purity pyridinic and pyrrolic N, possessing planar structures, reduce the energy barrier for O_2 adsorption, which leads to enhanced intrinsic electrocatalytic activity for the ORR [25,26]. Thus, the obtained electrocatalyst, possessing Fe-N_x, pyridinic, and pyrrolic N, is expected to display exceptional electrocatalytic properties. A high resolution Fe 2*p* spectrum was used to analyze

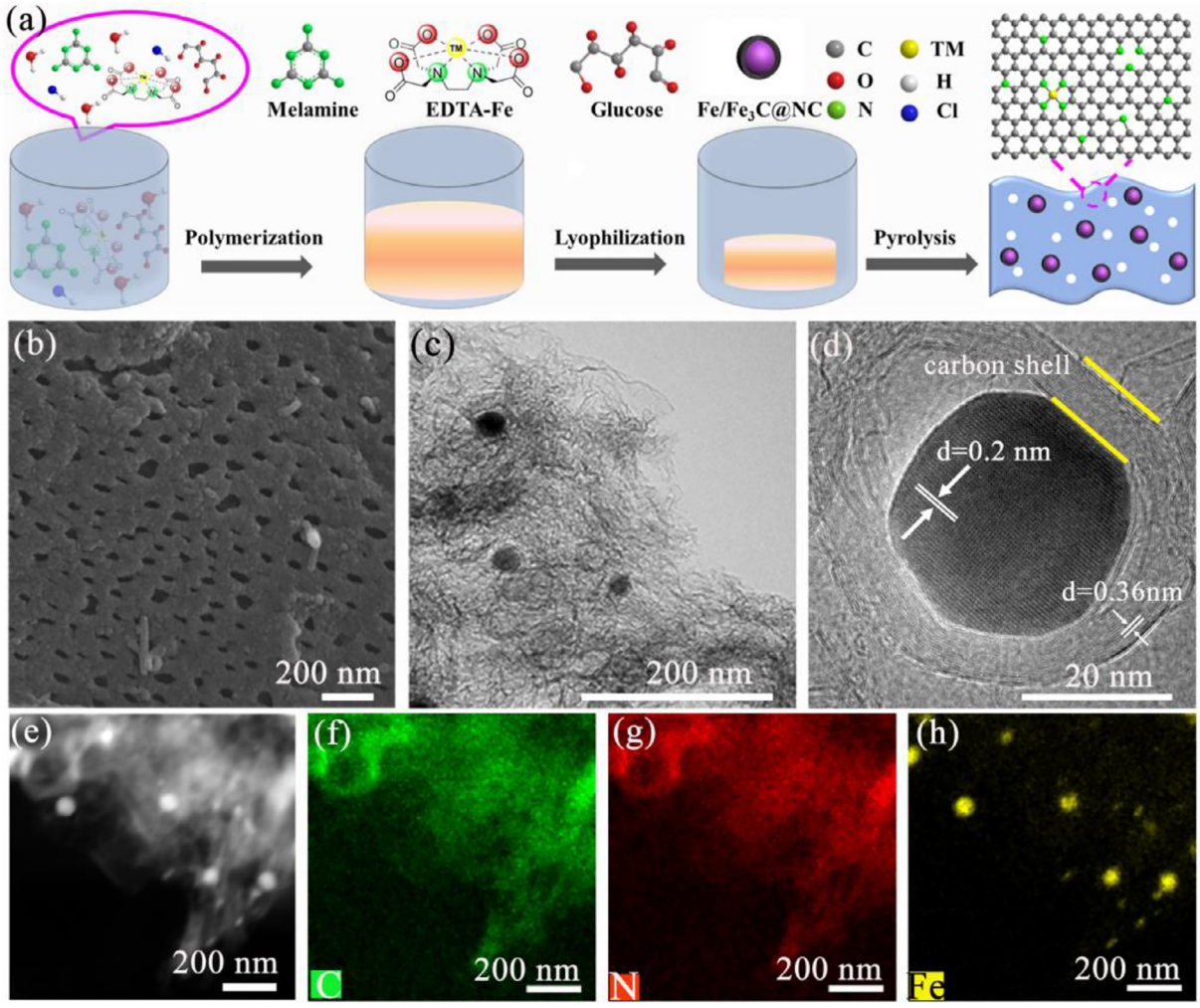

Fig. 1. (a) Synthetic scheme for Fe/Fe_3C@Fe-N_x-C. (b) SEM image, (c) TEM image, and (d) HRTEM image of Fe/Fe_3C@Fe-N_x-C synthesized at 950 °C. (e) HAADF-STEM image and the corresponding EDX maps of Fe/Fe_3C@Fe-N_x-C synthesized at 950 °C for (f) C, (g) N, and (h) Fe.

the chemical state of Fe and explore its vital contribution to the overall electrocatalytic performance. As exhibited in Fig. 2(d), the deconvoluted peaks centered at 706.9 eV and 720.0 eV corresponded to zero-valence Fe, suggesting the existence of metallic iron or carbide, respectively. The peaks located at approximately 710.9 eV and 724.1 eV were attributable to Fe in the Fe-N_x configuration [21,27]. These results further confirmed the coexistence of metallic Fe and Fe-N_x-C in the Fe/Fe_3C@Fe-N_x-C aerogel, both of which have been established as typical electrocatalytic active sites [28].

Subsequently, the electrocatalyst surface area and pore size distribution were analyzed, as well as its nitrogen adsorption–desorption characteristics. As shown in Fig. 2(e), the Fe/Fe_3C@Fe-N_x-C aerogel provides a specific surface area of 535 $m^2\ g^{-1}$. The N_2 sorption isotherms exhibited a pronounced hysteresis loop, implying the existence of a mesoporous structure formed by a 3D sheet-like framework, as confirmed by TEM [29]. Specifically, a Barrett-Joyner-Halenda (BJH) pore size distribution plot derived from the adsorption curve verified that the developed electrocatalyst possessed abundant mesopores, with pore diameters ranging from 5 to 50 nm (Fig. 2(f)). The porous structure affects the electrocatalytic performance significantly, and more importantly, mesopores facilitate the madefaction of the catalyst physical surface, and enhance active site utilization [30,31]. Thus, benefiting from the synergistic effect, bifunctional oxygen electrodes can provide excellent electrocatalytic activity and stability.

To investigate the electrocatalytic activity of the composite, its electrochemical performance was evaluated using the RDE method. The ORR data for the electrocatalysts pyrolyzed at different temperatures were obtained, to explore the impact of pyrolysis temperature on catalyst characteristics (Fig. S4). Fe/Fe_3C@Fe-N_x-C-950 exhibited the highest onset potential (1.0 V vs. RHE), and the most positive half-wave potential (0.90 V vs. RHE), compared to those of Fe/Fe_3C@Fe-N_x-C-900 (0.97 V and 0.88 V vs. RHE, respectively), and Fe/Fe_3C@Fe-N_x-C-1000 (0.95 V and 0.86 V vs. RHE, respectively). As evident from the TEM images (Fig. S2), the carbon matrix architecture experienced significant alterations with increasing pyrolysis temperature, and thin carbon nanosheets formed when the catalyst was annealed at 950 °C. The Raman spectroscopy results additionally suggested that the pyrolysis temperature influences the degree of graphitization and can thus be adjusted to optimize the electronic structure of an electrocatalyst. As indicated by the XPS results detailed in Table S1, Fig. S5, and Table S2, the N content declined with the increase of pyrolysis temperature. Interestingly, Fe/Fe_3C@Fe-N_x-C-950 exhibited a lower content of nitrogen species than Fe/Fe_3C@Fe-N_x-C-900, but superior electrocatalytic activity. This finding implies that increasing the content of appropriate active N species is more important than a high overall N doping content [32]. An important consideration is

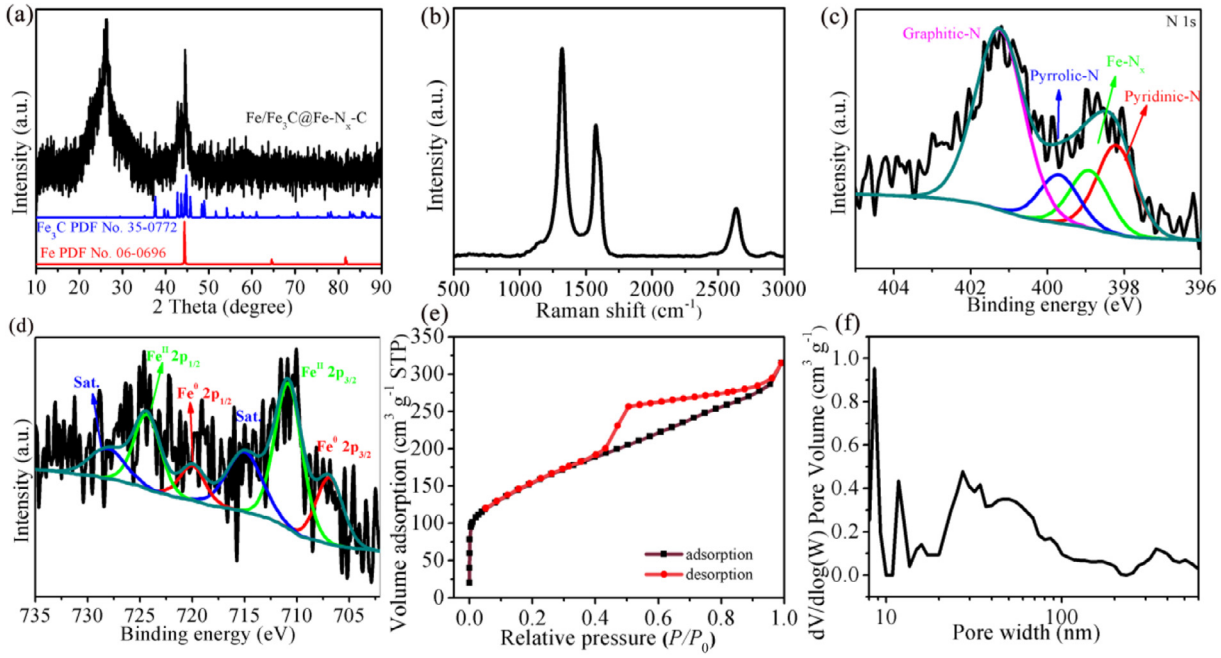

Fig. 2. (a) XRD patterns, (b) Raman spectrum, (c) N 1*s* high resolution XPS spectrum, (d) Fe 2*p* high-resolution XPS spectrum, (e) nitrogen ad- and desorption isotherms, and (f) derived pore size distribution of Fe/Fe_3C@Fe-N_x-C synthesized at 950 °C.

that high-temperature pyrolysis can enhance the conductivity and graphitization degree, which is beneficial for ORR performance. Therefore, the effective doping of active N species, optimal graphitization, and a porous structure are factors that enhance the electrocatalytic activity of Fe/Fe_3C@Fe-N_x-C.

Fig. 3(a) exhibits the ORR polarization curves of Fe/Fe_3C@Fe-N_x-C in O_2-saturated 0.1 M KOH medium. It is noteworthy that Fe/Fe_3C@Fe-N_x-C exhibited encouraging ORR activity with an E_{onset} (on-set potential) of 1.0 V, and a $E_{1/2}$ (half-wave potential) of 0.9 V. The electron-transfer number and kinetics of the optimized electrocatalyst were investigated next. Fig. 3(b) indicates that the limiting current densities increased with increasing rotation speeds, and that the E_{onset} remained constant at varying rotation speeds. Fig. 3(c) displays the Koutecky-Levich (K-L) plots of Fe/Fe_3-C@Fe-N_x-C, which feature distinct linear relationships at various potentials. The electron transfer number calculated from the K-L plot was ~3.74, indicating preference for the four-electron process in the ORR. The Tafel plots (Fig. 3(d)) show that the Fe/Fe_3C@Fe-N_x-C sample presented the smallest slope of 56 mV dec^{-1}, compared to those of N-C (141 mV dec^{-1}), and benchmark Pt/C (64 mV dec^{-1}),

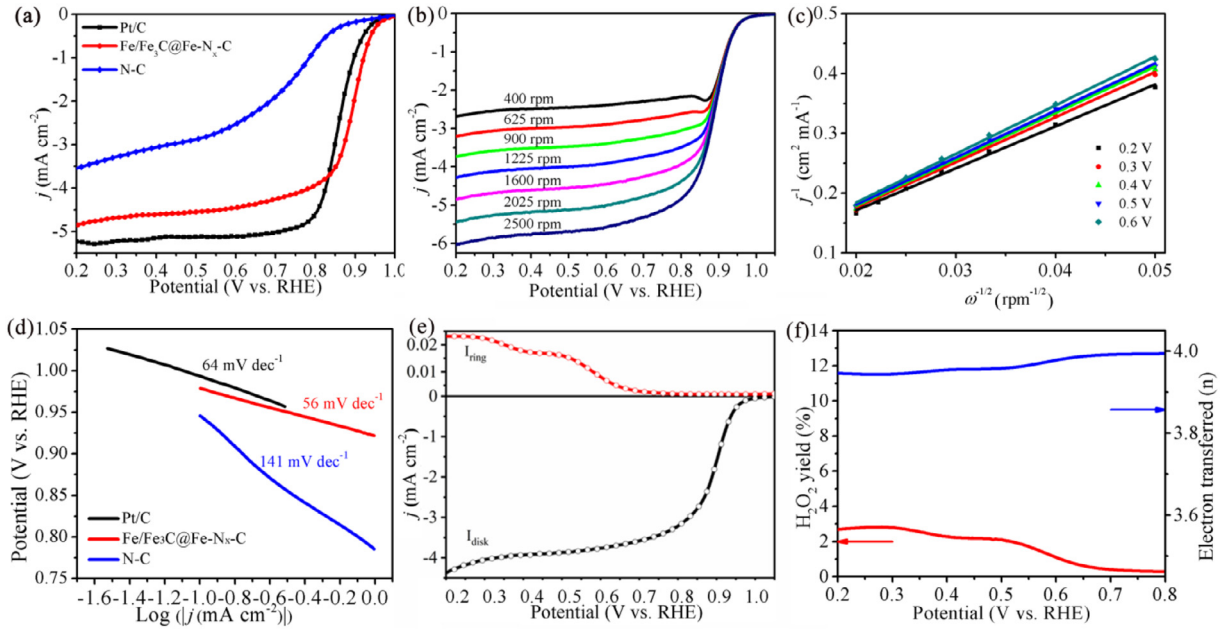

Fig. 3. (a) ORR polarization curves of Pt/C, Fe/Fe_3C@Fe-N_x-C and N-C. Scan rate: 5 mV s^{-1}; rotation rate: 1600 rpm. (b) LSV curves of Fe/Fe_3C@Fe-N_x-C in O_2-saturated 0.1 M KOH at various rotation speeds. Scan rate: 5 mV s^{-1}. (c) K-L plots of Fe/Fe_3C@Fe-N_x-C at various potentials. (d) Tafel slopes of Fe/Fe_3C@Fe-N_x-C, N-C and Pt/C. (e) RRDE LSV curves of Fe/Fe_3C@Fe-N_x-C at a rotation rate of 1600 rpm; scan rate: 5 mV s^{-1}. (f) H_2O_2 yield and electron transfer number of Fe/Fe_3C@Fe-N_x-C at 1600 rpm.

further verifying its superior ORR activity. The electron transfer number measured by the RRDE technique during ORR (Fig. 3(e)) was in agreement with the value obtained from the K-L plots. Notably, H_2O_2 yields were consistently below 3% in the potential range of 0.2–0.8 V (vs. RHE), implying complete reduction of O_2 via the four-electron process (Fig. 3(f)) [33]. Stability and tolerance to methanol are likewise important parameters for evaluating the utility of developed electrocatalysts. To assess electrocatalyst stability and resistance to methanol crossover, chronoamperometric measurements were performed in O_2-saturated 0.1 M KOH solution with an RDE rotation speed of 1600 rpm. The Fe/Fe_3C@Fe-N_x-C electrocatalyst obtained at 950 °C displayed excellent stability, even beyond 40,000 s (Fig. S6(a)). In contrast, benchmark Pt/C exhibited severely degraded durability over time. Fe/Fe_3C@Fe-N_x-C morphology was analyzed by TEM after its 40,000 s ORR durability test, wherein no obvious differences were observed in the electrocatalyst morphologies prior to and after the test (Fig. S7), suggesting excellent catalyst stability. Unlike the benchmark Pt/C catalyst, Fe/Fe_3C@Fe-N_x-C displayed excellent tolerance to methanol (Fig. S6(b)). Overall, the as-developed Fe/Fe_3-C@Fe-N_x-C electrocatalyst exhibited outstanding ORR performances, a preference for the four-electron transfer process, excellent stability, and high methanol tolerance.

The obtained Fe/Fe_3C@Fe-N_x-C electrocatalyst was additionally employed as a water oxidation electrocatalyst to evaluate its OER activity. As shown in Fig. 4(a), when the current density reaches 10 mA cm^{-2}, the Fe/Fe_3C@Fe-N_x-C electrocatalyst obtained at 950 °C presents a significantly lower potential (1.63 V) than that obtained for N-C (1.72 V), demonstrating promising OER activity. Additionally, the Tafel slope for the Fe/Fe_3C@Fe-N_x-C electrocatalyst (92 mV dec^{-1}) was considerably smaller than that of N-C (292 mV dec^{-1}), signifying superior reaction kinetics (Fig. 4(b)). Fig. S8 presents the OER durability test results for Fe/Fe_3C@Fe-N_x-C, obtained by electrolysis at a static overpotential; here, current density/time dependence indicated negligible degradation after 20,000 s. The TEM image (Fig. S9) of Fe/Fe_3C@Fe-N_x-C recorded after the OER durability test demonstrated no obvious morphology changes when compared to its morphology prior to the test, implying outstanding stability. No significant differences in the chemical composition were noted in the high-resolution N 1*s* spectra of Fe/Fe_3C@Fe-N_x-C recorded before and after the OER stability test, indicating favorable chemical and structural stability during the OER (Fig. S10). To evaluate the OER efficiency of Fe/Fe_3-C@Fe-N_x-C, the RRDE technique was performed in O_2 or N_2-saturated KOH electrolyte. As depicted in Fig. 4(c), monitoring of the negligible ring current density suggested that the desired four-electron process was preferable for the OER [34]. To verify that the detected disk current density arises from the gaseous product of the electrode reaction, rather than from side reactions, the Faradaic efficiency (OER) of Fe/Fe_3C@Fe-N_x-C was assessed (Fig. 4(d)). Ring electrode potential was maintained at 0.4 V (vs. RHE) to detect evolved O_2 on the disk electrode, and a ring current of approximately 110 μA was detected when a constant current of 300 μA was applied to the disk electrode. Therefore, a high Faradic efficiency of ~100% was achieved, confirming that the tested current originated exclusively from the OER [35].

It has been established that the smaller the ΔE value (difference between the OER potential at 10 mA cm^{-2} and the ORR $E_{1/2}$ potential), the higher the electrocatalytic activity of a bifunctional oxygen electrode [36]. Fig. S11 illustrates the exceptional ORR and OER activities of Fe/Fe_3C@Fe-N_x-C, and its small ΔE value of 0.74 V, which was found to be superior to that of a number of reported outstanding bifunctional oxygen electrocatalysts, including Mn_xO_y/N-carbon (0.87 V) [37], FeNi-N-carbon (0.81 V) [1], Co-N co-doped hollow carbon sphere (0.856 V), [36] and N, S, O-carbon nanosheets (0.88 V) [38]. Based on the above findings, it can be concluded that the obtained Fe/Fe_3C@Fe-N_x-C electrocatalyst

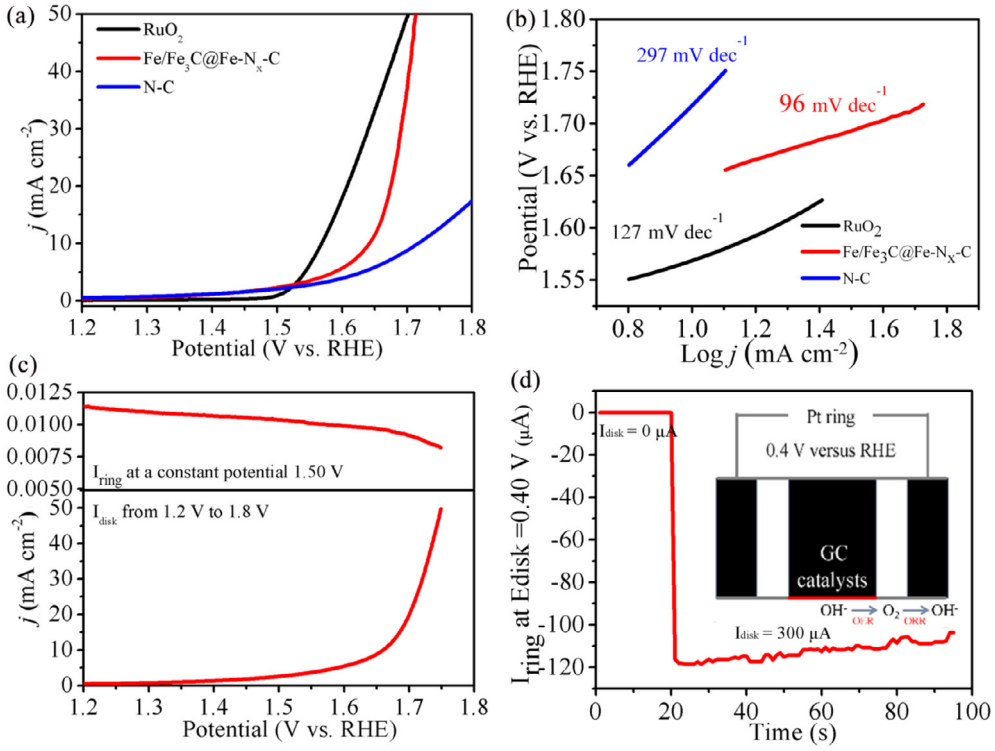

Fig. 4. (a) OER polarization curves of Fe/Fe_3C@Fe-N_x-C, RuO_2 and N-C in O_2-saturated 1.0 M KOH electrolyte with a scan rate of 5 mV s^{-1} (1600 rpm). (b) Tafel plots of Fe/Fe_3C@Fe-N_x-C, RuO_2 and N-C. (c) RRDE measurement of Fe/Fe_3C@Fe-N_x-C in O_2-saturated 1.0 M KOH electrolyte at a rotation speed of 1600 rpm, and a scan rate of 5 mV s^{-1}. (d) Faraday efficiency characterization of Fe/Fe_3C@Fe-N_x-C in N_2-saturated 1.0 M KOH electrolyte (The inset represents the Faraday efficiency testing mechanism of the RRDE).

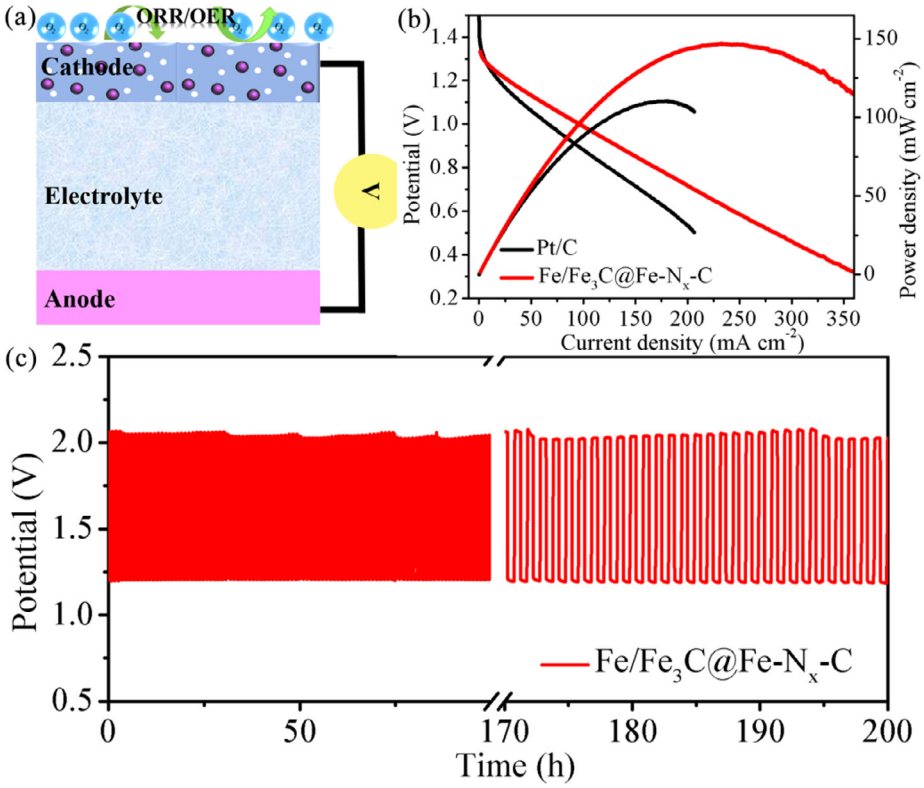

Fig. 5. (a) Schematic of Zn-air battery configuration. (b) Power density and discharge polarization curves of the Zn-air battery based on the Fe/Fe_3C@Fe-N_x-C air cathode and based on Pt/C. (c) Discharge-charge cycling curve of the rechargeable Zn-air battery at a current density of 5 mA cm^{-2}.

exhibited a promising performance for the development of bifunctional oxygen electrocatalysts.

Considering the remarkable electrocatalytic activity and exceptional robustness of Fe/Fe_3C@Fe-N_x-C towards ORR and OER, a rechargeable Zn-air battery was constructed, employing zinc foil as the anode and Fe/Fe_3C@Fe-N_x-C as the cathode (Fig. 5(a)). As shown in Fig. 5(b), the discharge curve and corresponding power densities of the assembled Zn-air battery exhibited promising electrocatalyst activity. The maximum power density of the fabricated battery was confirmed to be 147 mW cm^{-2}, which was considerably higher than that of Pt/C (120 mW cm^{-2}). Significantly, a high current density was observed for the assembled Zn-air battery, outperforming the commercial Pt/C-based counterpart (Fig. S12). The galvanostatic discharge–charge cycling curves of the assembled Zn-air battery (Fig. 5(c)) further imply its excellent reversibility over 200 cycles at a high discharge/charge current density of 5 mA cm^{-2} (1 h per cycle) with a small discharge/charge voltage gap of ~0.87 V. The overall results reveal the significant potential of the Fe/Fe_3C@Fe-N_x-C electrocatalyst for application in rechargeable Zn-air batteries, based on its outstanding reactivity and stability.

4. Conclusions

In summary, we developed a facile and cost-efficient sol–gel synthetic approach for the fabrication of Fe/Fe_3C@Fe-N_x-C bifunctional oxygen electrocatalysts. The electrocatalyst exhibited 3D meso- and microporous morphology, consisting of Fe/Fe_3C nanoparticles encapsulated by ultrafine onion-like carbon shells and a nanosheet-like Fe, N-co-doped carbon aerogel. These unique hierarchical structural characteristics endowed the catalyst with abundant accessible reversible oxygen electrocatalytic sites, and gave rise to superb electrocatalytic activity, in terms of positive E_{onset} potential, a large half-wave potential, superb durability for ORR, and a low potential at j = 10 mA cm^{-2} for OER. The as-fabricated rechargeable Zn-air battery, employing Fe/Fe_3C@Fe-N_x-C as the cathode, afforded a high peak power density of 147 mW cm^{-2} and excellent stability over 200 cycles at 5 mA cm^{-2} with a narrow discharge/charge voltage gap of ~0.87 V. Consequently, in addition to the generation of an efficient low-cost bifunctional oxygen electrocatalyst, this study features a facile and rational strategy applicable to the development of transition-metal-based catalysts for electrochemical reactions and practical energy conversion applications.

Declaration of Competing Interest

The authors declare that they have no known competing financial interests or personal relationships that could have appeared to influence the work reported in this paper.

Acknowledgments

This work was supported financially by the National Natural Science Foundation of China, China (Grant No. 51702180, 51572136, 91963113, 21703116, 51372127, 51873096), The Scientific and Technical Development Project of Qingdao, China (Grant No.18-2-2-52-jch), The Taishan Scholar Advantage and Characteristic Discipline Team of Eco Chemical Process and Technology, The Natural Science Foundation of Hebei Province (B2019204009).

Appendix A. Supplementary data

Supplementary data to this article can be found online at https://doi.org/10.1016/j.jechem.2020.07.048.

References

[1] L. Yang, X. Zeng, D. Wang, D. Cao, Energy Storage Mater. 12 (2018) 277–283.
[2] K. Kordek, L. Jiang, K. Fan, Z. Zhu, L. Xu, M. Al-Mamun, Y. Dou, S. Chen, P. Liu, H. Yin, P. Rutkowski, H. Zhao, Adv. Energy Mater. 9 (2019) 1802936–1802944.
[3] C. Hang, J. Zhang, J. Zhu, W. Li, Z. Kou, Y. Huang, Adv. Energy Mater. 8 (2018) 1703539–1703547.
[4] J. Zhang, Z. Zhao, Z. Xia, L. Dai, Nat. Nanotechnol. 10 (2015) 444–452.
[5] L. Bu, N. Zhang, S. Guo, X. Zhang, J. Li, J. Yao, T. Wu, G. Lu, J.Y. Ma, D. Su, X. Huang, Science 354 (2016) 1410–1414.
[6] D.S. He, D. He, J. Wang, Y. Lin, P. Yin, X. Hong, Y. Wu, Y. Li, J. Am. Chem. Soc. 138 (2016) 1494–1497.
[7] Y. Xiong, Y. Yang, X. Feng, F.J. DiSalvo, H.D. Abruna, J. Am. Chem. Soc. 141 (2019) 4412–4421.
[8] Z. Wu, R. Liu, J. Wang, J. Zhu, W. Xiao, C. Xuan, W. Lei, D. Wang, Nanoscale 8 (2016) 19086–19092.
[9] X.F. Lu, Y. Chen, S. Wang, S. Gao, X.W. Lou, Adv. Mater. 31 (2019) 1902339–1902347.
[10] Z. Du, P. Yu, L. Wang, C. Tian, X. Liu, G. Zhang, H. Fu, Sci. China. Mater. 63 (2019) 327–338.
[11] L. Ma, S. Chen, Z. Pei, Y. Huang, G. Liang, F. Mo, Q. Yang, J. Su, Y. Gao, J.A. Zapien, C. Zhi, ACS Nano 12 (2018) 1949–1958.
[12] S. Wang, M. Qiao, Y. Wang, Q. Wang, G. Hu, X. Mamat, S. Zhang, Angew. Chem. 59 (2019) 2688–2694.
[13] Y. Chen, S. Ji, Y. Wang, J. Dong, W. Chen, Z. Li, R. Shen, L. Zheng, Z. Zhuang, D. Wang, Y. Li, Angew. Chem. Int. Ed. 56 (2017) 6937–6941.
[14] D. Deng, L. Yu, X. Chen, G. Wang, L. Jin, X. Pan, J. Deng, G. Sun, X. Bao, Angew. Chem. Int. Ed. 52 (2013) 371–375.
[15] G. Wu, K.L. More, C.M. Johnston, P. Zelenay, Science 332 (2011) 443–447.
[16] L. Chong, J. Wen, J. Kubal, F.G. Sen, J. Zou, J. Greeley, M. Chan, H. Barkholtz, W. Ding, D.J. Liu, Science 362 (2018) 1276–1281.
[17] H. Khani, N.S. Grundish, D.O. Wipf, J.B. Goodenough, Adv. Energy Mater., 10 (2019) 1903215–190324.
[18] X. Cui, P. Ren, D. Deng, J. Deng, X. Bao, Energy Environ. Sci. 9 (2016) 123–129.
[19] D. Liu, X. Li, S. Chen, H. Yan, C. Wang, C. Wu, Y.A. Haleem, S. Duan, J. Lu, B. Ge, P. M. Ajayan, Y. Luo, J. Jiang, L. Song, Nat. Energy 4 (2019) 512–518.
[20] X. Zhao, S.C. Abbas, Y. Huang, J. Lv, M. Wu, Y. Wang, Adv. Mater. Interfaces 5 (2018) 1701448–1701454.
[21] W.J. Jiang, L. Gu, L. Li, Y. Zhang, X. Zhang, L.J. Zhang, J.Q. Wang, J.S. Hu, Z. Wei, L. J. Wan, J. Am. Chem. Soc. 138 (2016) 3570–3578.
[22] D. Xia, X. Yang, L. Xie, Y. Wei, W. Jiang, M. Dou, X. Li, J. Li, L. Gan, F. Kang, Adv. Funct. Mater. 174 (2019) 1906174–1906183.
[23] S.H. Ahn, X. Yu, A. Manthiram, Adv. Mater. 29 (2017) 1606534–1606543.
[24] K. Mamtani, D. Jain, D. Dogu, V. Gustin, S. Gunduz, A.C. Co, U.S. Ozkan, Appl. Catal. B-Environ 220 (2018) 88–97.
[25] D. Yu, Q. Zhang, L. Dai, J. Am. Chem. Soc. 132 (2010) 15127–15129.
[26] R.A. Sidik, A.B. Anderson, N.P. Subramanian, S.P. Kumaraguru, B.N. Popov, J. Phys. Chem. B 110 (2006) 1787–1793.
[27] X. Sun, P. Wei, S. Gu, J. Zhang, Z. Jiang, J. Wan, Z. Chen, L. Huang, Y. Xu, C. Fang, Q. Li, J. Han, Y. Huang, Small 16 (2020) 1906057–1906066.
[28] X. Huang, Y. Zhang, H. Shen, W. Li, T. Shen, Z. Ali, T. Tang, S. Guo, Q. Sun, Y. Hou, ACS Energy Lett. 3 (2018) 2914–2920.
[29] M. Graglia, J. Pampel, T. Hantke, T.P. Fellinger, D. Esposito, ACS Nano 10 (2016) 4364–4371.
[30] S.H. Lee, J. Kim, D.Y. Chung, J.M. Yoo, H.S. Lee, M.J. Kim, B.S. Mun, S.G. Kwon, Y. E. Sung, T. Hyeon, J. Am. Chem. Soc. 141 (2019) 2035–2045.
[31] H.T. Chung, D.A. Cullen, D. Higgins, B.T. Sneed, E.F. Holby, K.L. More, P. Zelenay, Science 357 (2017) 479–484.
[32] M. Li, L. Zhang, Q. Xu, J. Niu, Z. Xia, J. Catal. 314 (2014) 66–72.
[33] J. Zhang, L. Qu, G. Shi, J. Liu, J. Chen, L. Dai, Angew. Chem. Int. Ed. 55 (2016) 2230–2234.
[34] S. Zhao, Y. Wang, J. Dong, C.-T. He, H. Yin, P. An, K. Zhao, X. Zhang, C. Gao, L. Zhang, J. Lv, J. Wang, J. Zhang, A.M. Khattak, N.A. Khan, Z. Wei, J. Zhang, S. Liu, H. Zhao, Z. Tang, Nat. Energy 1 (2016) 16184–16193.
[35] J. Suntivich, K.J. May, H.A. Gasteiger, J.B. Goodenough, Y. Shao-Horn, Science 334 (2011) 1383–1385.
[36] S. Cai, Z. Meng, H. Tang, Y. Wang, P. Tsiakaras, Appl. Catal. B-Environ. 217 (2017) 477–484.
[37] J. Masa, W. Xia, I. Sinev, A. Zhao, Z. Sun, S. Grutzke, P. Weide, M. Muhler, W. Schuhmann, Angew. Chem. Int. Ed. 53 (2014) 8508–8512.
[38] K. Qu, Y. Zheng, S. Dai, S.Z. Qiao, Nano Energy 19 (2016) 373–381.